Contents

Part I

ActiveAx

Chapter 1

Scan/rescan reproducibility in the corpus callosum and spinal cord

1.1 Introduction

In the previous chapter we have presented a implementation of our $a\mathcal{SF}$ protocols on a clinical system. We found that the 25 minute long $a\mathcal{SF}$ acquisition can produce comparable results to the 3 times longer $\mathcal{OI}$ method. Our initial work was focussed only on the optimisation of the acquisition protocol. However, clerly other non-diffusion related imaging parameters, such as accurate positioning or spatial resolution, also contribute significantly to the goodness of the parameter estimates coming from our protocol. In this chapter we address several shortcomings of the initial $a\mathcal{SF}$ setup. Our main aim is to improve SNR and spatial resolution of our dataset in order to maximise accuracy and reproducibility of our microstructure maps.

In detail, we make the following changes compared to the $a\mathcal{SF}$ experiment described in in Chapter **??**:

1. We use of a small field-of-view (FOV) imaging sequence to increase both image resolution and SNR.

2. We develop a new method to better align the image volume with the dominant fibre direction of the CC using fast DTI tractography directly on the scanner console.

3. We extend the signal model used in the optimisation and fitting to allow the use of shortest available echo time (TE) for different combination of diffusion gradient pulse duration (δ) and diffusion time (Δ). Furthermore we increase the nominal maximal gradient strength to 87mT/m using the the modified scanner software we developed for the QSI study in Chapter **??**. The combined effect lower TE and stronger gradient will increase SNR and aid the performance of the parameter fitting routine.

We analyse our new imaging pipeline in 5 healthy volunteers, who were scanned at two different timepoint to assess both intra- and inter-subject reproducibility.

Furthermore we propose the first implementation of our $a\mathcal{SF}$ protocol in the cervical spine and test it in one healthy volunteer.

1.2 Methods & Experiments

Protocol optimisation

We use the same $a\mathcal{SF}$ optimisation as described in Chapter **??**, but with one modification: we extend the tissue model to include an additional T2 decay factor that accounts for signal loss in the DWI with respect to the TE on a per-acquisition basis. For simplicity, we assume here a mono-exponential T2 decay of the signal. Previously, the TE was governed by the maximum TE in the whole protocol. This modification now allows the dynamic use of TEs for different (δ, Δ) settings in the protocol optimisation. This has the advantage of effectively reducing the TE in the low DWI acquisition, which improves greatly the SNR in those acquisitions.

We carry out the optimisation using as before, assuming T2=70ms, which is typical for white matter (WM) in the CC (). We also use the scanner software modification we described in Chapter **??**, which allows to combine several orthogonal 62mT/m-gradients to increase the maximum gradient strength to 87mT/m. To improve directional resolution required for the fit of the diffusion direction, we add a single shell DTI acquisition (max b=800s/mm^2, 1 b=0, 16 uniformly distributed directions) to the optimised protocol. The full set of parameters is given in Table 1.1.

Table 1.1: Optimised protocol parameters for the $a\mathcal{SF}$ method with variable TEs

|	δ [ms]	Δ [ms]	G [mT/m]	TE [s]
1b0	0	0	0	23
1b0 + 5$\parallel$	8	22	78	46
1b0 + 14$\perp$	13	20	87	54
1b0 + 7$\perp$	22	56	48	96
1b0 + 26$\perp$	23	29	87	73
1b0 + 20$\perp$	27	50	63	93
1b0 + 11$\perp$	35	42	81	93
1b0 + 16 DTI	b=800 s/mm^2			47
	total scan time 35min			

### 1.2.1 CC reproducibility study

Data acquisition

We recruited 5 healthy volunteers (3 female, 2 male, mean age=28 $\pm$) to be scanned on a Philips Achieva 3TX scanner. All subjects were recalled for a second scan on a different day to assess the intra-subject reproducibility of the experiment. In each scan session we acquire a the optimised $\mathcal{SF}$ DWI protocol with following scan parameters: voxel size: 1x1x4mm^3, FOV=96x96mm^2,

TR=6000ms, 2 averages, using an outer-volume suppressed ZOOM acquisition (Wilm et al., 2007) to avoid fold-over artifacts.

The previous experiments have shown that our $\mathcal{SF}$ methods benefit from accurate alignment of the gradient scheme with respect to the dominant fibre direction. While standard T2w localizers are adequate to align the scan volume to anatomical reference, it offers no information about the WM fibre orientation. To aid slice positioning, we acquire a fast DTI scan in addition to the conventional scout scans. The scout-DTI imaging parameters are as follows: voxelsize=2x2x4mm^3, 16 slices, FOV=232x232 mm^2, TE=78ms, TR=4200ms, 6 non-colinear diffusion weighted directions (b=1000) plus one non-diffusion weighted image. Total scan time of the scout DTI scan is 57 seconds. We use the PRIDE tools directly on the scan console to place a ROI in the mid-sagittal slice of the CC and perform FACT tractography on the DTI dataset (FA threshold=0.45, angle threshold=YY). The tracts are then overlayed on the colour-coded FA map, rasterised, and resliced to obtain a new 1x1x1 image volume. To plan the final $\mathcal{SF}$ scan, we use the axial and coronal views of the tractography results to adjust the angulation of the axial slices with respect to the observed tracts. Figure 1.1 shows an example of the final slice alignment based on both the structural localizer scan and tractography results. Since the whole scout-DTI processing is performed on the scanner console, the additional scan setup time by acquiring analysing the scout-DTI scan is kept to a minimum.
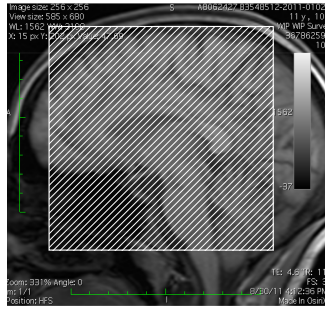
(a) Sagittal localizer
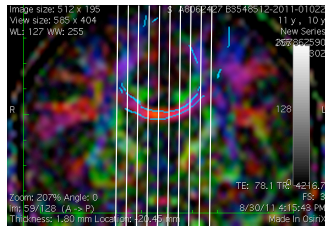
(b) Coronal FA map overlayed with tractography results (cyan lines)
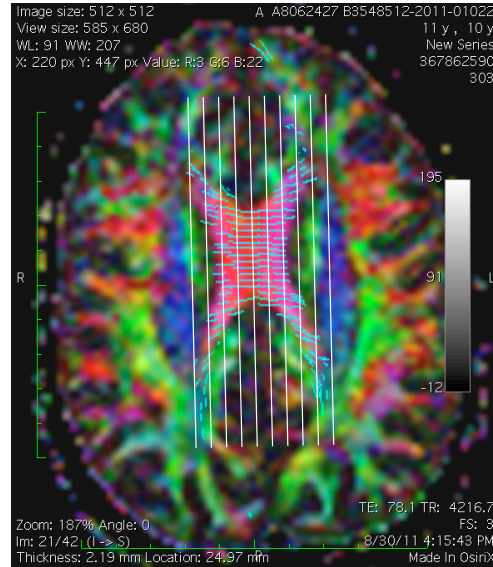
(c) Axial FA map with overlayed tractography results (cyan lines)

Figure 1.1: Positioning of small FOV scans in white, overlayed on a sagittal scout image (a) and axial and coronal DTI tractography results (b&c).

Post-processing

We compensate for motion during the acquisition by aligning all scan volumes to the first b=0 image using the block-wise rigid registration algorithm (Ourselin et al., 2001) implemented in (Modat et al., 2010). However, since the diffusion weighted images provide little contrast in non-coherently aligned WM tissue, we only register the interleaved b=0 images and apply the estimated transformation matrix to the subsequent intermediate b>0 images.

To ensure anatomical correspondence between scan and rescan, we then register the rescan dataset to the scan dataset (using rigid registration) using the transformation estimates from registering the first b=0 images of the two datasets. The transformation matrices for intra-scan motion and scan/rescan alignment are combined before applying them to the dataset to avoid unnecessary multiple interpolations. The data is then smoothed using the Unbiased-Non-Local-Means filter (Tristán-Vega et al., 2012) with a small filter radius of $3 \times 3 \times 4mm^3$.

Data analysis

We use the same fitting procedure as outlined in the previous chapters. However since we allowed for variable TE in each acquisition, we need to account for the resulting differences in T2 single decay within the data. We therefore estimate the voxel-wise mono-exponential decay curve using a linear regression model based on the non-diffusion-weighted acquisitions. The predicted MR signal S from the tissue model is then adjusted based on its TEs by:

$$S' = S * exp(TE/T2). \qquad (1.1)$$

The adjusted signal S' is then used to compute the rician log-likelihood with the observed signal as before. As in the previous studies, we compute the posterior distributions of the model parameters using an MCMC method on a voxel-by-voxel basis. From the mean of the posterior distribution we compute the the axon diameter index a and axonal density index ρ=f$/\pi/a^2$. In addition we also fitted the diffusion tensor to the 16-direction DTI data and derive the principal eigenvectors $v1$–$v3$ and scalar maps of FA, MD, AD, RD. All fitting is implemented using the Camino toolkit (Cook et al., 2006).

ROI analysis

In each subject we manually segmented the CC on the mid-sagittal slice. We then remove all voxels from the CC mask with FA<0.5 to exclude voxels with more than one single fibre orientation or significant CSF contamination. We further exclude voxel from the analysis where v1 deviated more than 10 degrees from the left-right fibre orientation we assumed in the protocol optimisation. The CC segmentation is then divided in 10 equidistant regions along the anterior-posterior baseline similar to Aboitiz et al. (1992). Figure 1.2 shows an example of the CC subdivision in one subject. Mean a and ρ indices are then computed for each CC subdivision in each of the 10 datasets. Scan/rescan agreement is assessed visually as well as it is quantified by computing the intraclass correlation coefficient (ICC) (Shrout & Fleiss, 1979) over the whole CC and in each region of interest (ROI). To investigate the correlation between DTI
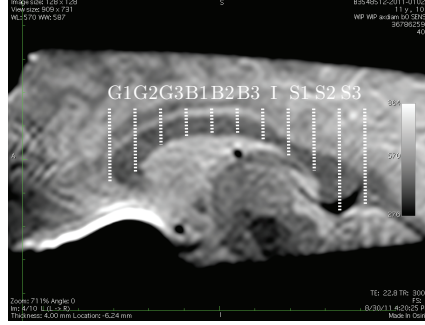
Figure 1.2: Example of CC subdivision scheme overlayed on the midsagittal slice of a b=0 image in one volunteer. The ROIs divide the CC in genu (G1–G3), midbody (B1–B3), isthmus region (I) and splenium (S1–S3).

metrics and a and ρ, we pool all values in the CC ROI from all subjects separately for scan and rescan and report the robust correlation coefficient(Huber, 1996). All statistical processing was performed using the software R(R Core Team, 2012) with packages 'ICC'(Wolak et al., 2011) and 'robust'(Wang et al., 2012).

1.2.2 SC experiment

Data acquisition

We performed the scans our $a\mathcal{SF}$ in one healthy volunteers (41YO female). The $\mathcal{SF}$ DWI protocol wasacquired with following scan parameters: voxel size: 1x1x5mm3, FOV=64x64mm^2, cardiac gated, TR=5RR, using the outer-volume suppressed ZOOM acquisition (Wilm et al., 2007) in the CC. We chose the 32-channel head coil to perform the scans as we found that it offers superior SNR in the cervical cord region than the dedicated 16-channel head-neck coil alternative.Scan were acquired between the discs C1/2 and C3/4, although severe motion artifacts made it necessary to exclude all slices except the 3 most caudal slices.

1.3 Results

Axon diameter and axon density indices in the CC

Figure 1.3 shows side-by-side scan/rescan maps of a and ρ for all five subjects. Figure 1.4 summarizes the mean a and ρ parameters measured in each ROI for all five subjects. In all subjects we can clearly see the variation along AP we expect from previous experiment and earlier studies (Alexander et al., 2010). Furthermore, in comparison with those earlier results, our maps appear considerably less noisy and show improved contrast between different CC regions. Consistent with our previous results, we estimate values of a in the range of 5–15μm. The largest a estimates are found in the midbody of the CC. The smallest a values are found in the splenium $<8\mu m$ and the anterior part of the genu (9–11μm). The axon density index ρ is reciprocal to the a trends, with

ρ being largest in the anterior genu and posterior splenium regions and smallest in the body and isthmus of the CC. The a and ρ pattern we observe here agrees very well with the microstructure that is seen in excised human CC tissue samples.

Unlike in the previous experiments, the high spatial resolution here provides a large number of voxels that are completely contained in the CC. As a consequence, the CC can be easily distinguished from surrounding tissue and the tissue parameter estimates are less influenced by CSF contamination, particularly in the thinning part of the CC (B3–S1). This is beneficial for subjects with smaller CC such as found in s2 & s3, but becomes even more important in view of future applications in patients with neurological diseases such as MS or Alzheimers disease, who often suffer from severe CC atrophy.
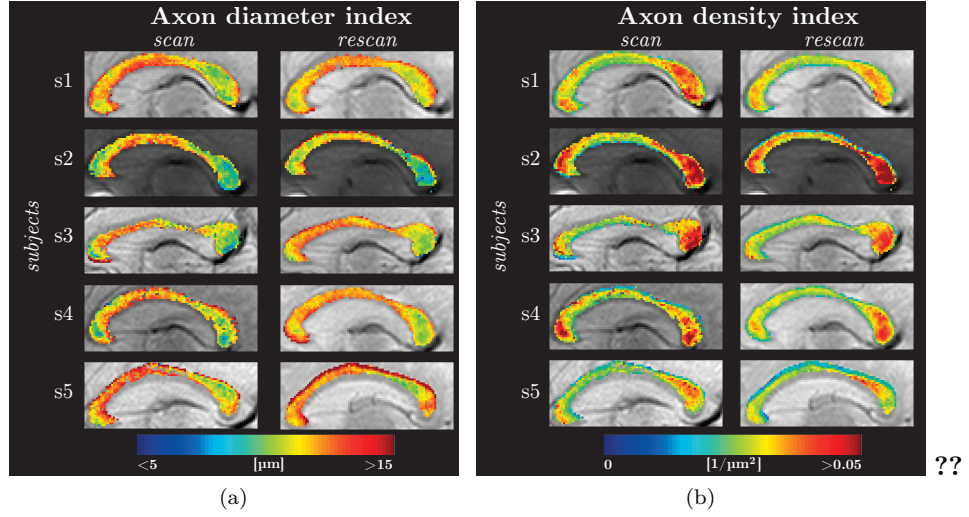

Figure 1.3: Individual maps of a and ρ in the sagittal slice for each subject for the scan and rescan experiments.

Inter- & Intra-subject reproducibility

Results in Figure 1.3 and Figure 1.4 suggest good ROI-wise consistency of the parameter maps between the five subjects. Figure 1.5, also shows that the average taken over all 5 subjects for the scan and rescan experiment agree very well with each other, both in the average trend as well as in the observed standard deviation. Moreover, both a and ρ show very little variation from the mean over all subjects. Inter-subject variation is lower in the mid-body and the proximal genu regions (G2–G3) than in the more distal anterior and posterior regions. The Bland-Altman plots shown in Figure 1.6 show good scan/rescan variation independent of parameter estimate with the majority of ROI estimates within the confidence interval of 1.5 standard deviations. In a minority of ROIs we see outliers with scan/rescan large variation. This appears to be related to large axon density estimates, which appear more unstable than smaller ρ values. Those outliers appear mostly in the most distal G1 and S3 regions. Such

large variations might indicate cardiac pulsation artifacts as these regions are closest to the adjacent Arteria Cerebralis. In *a* the scan/rescan variability appears more independent of the actual estimation values.

Table 1.2 presents the ICC for whole CC and individual ROIs. For both *a* and ρ, we find the scan/rescan agreement being 'moderate' or better for both whole CC values and most ROIs. As noted before, the lowest ICC values are found in boundary regions (G1) or in the thin proximal part of the CC, which are most affected by imaging and analysis artefacts. Both Bland-Altman analysis as well as the ICC suggest that estimated values in those ROIs appear more prone to error and must be interpreted with caution.
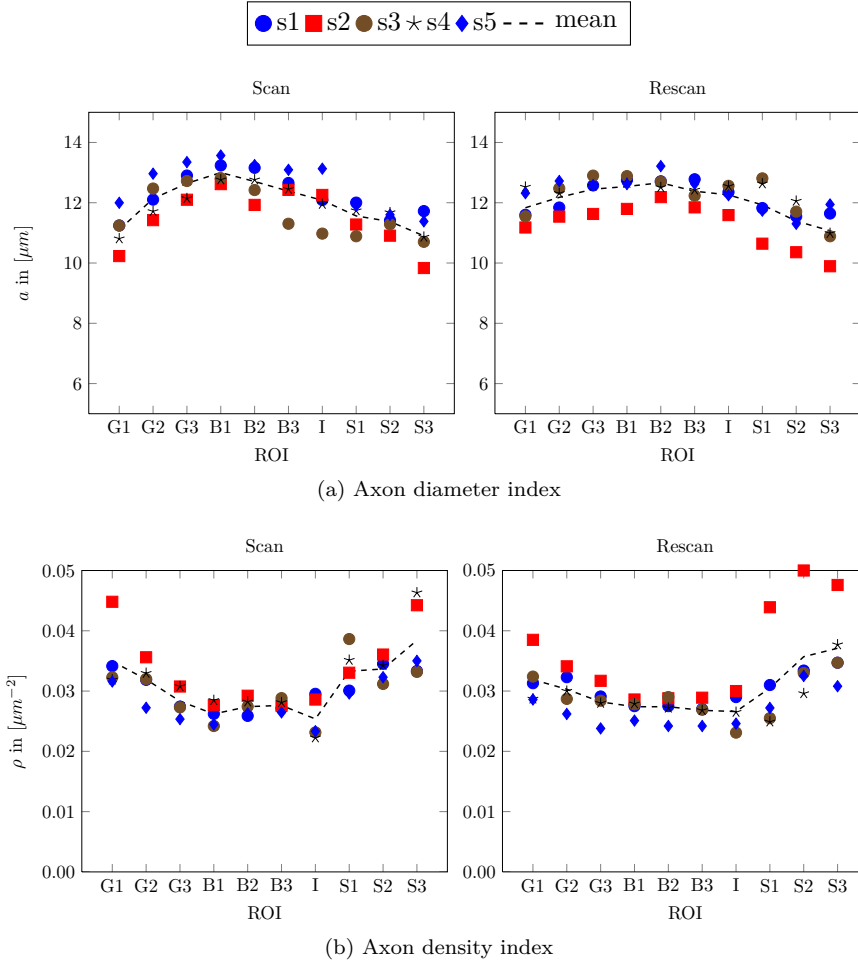

(a) Axon diameter index

(b) Axon density index

Figure 1.4: Scatter plots of axon diameter (*a*) and axon density (ρ) indices in all 5 subjects in individual ROIs. The dashed line shows the average over all subjects.

Correlation with DTI metrics

Figure 1.7 presents the correlation between the standard DTI metrics and the
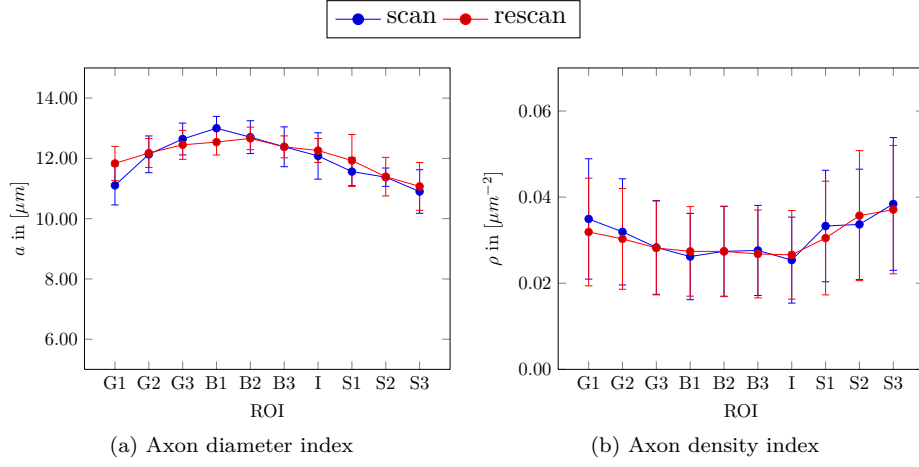
(a) Axon diameter index

(b) Axon density index

Figure 1.5: Average and standard deviation a and ρ over the whole group of 5 subjects for different ROIs.

Table 1.2: ICC values for whole CC and individual ROIs for a and ρ estimates.

	whole CC	G1	G2	G3	B1	*Individual ROIs* B2	B3	I	S1	S2	S3
a	0.66 ■	0.14 ■	0.83 ■	0.56 ■	0.14 ■	0.81 ■	0.46 ■	-0.25 ■	-0.07 ■	0.70 ■	0.94 ■
ρ	0.79 ■	0.74 ■	0.77 ■	0.78 ■	0.44 ■	0.59 ■	0.34 ■	0.79 ■	-0.14 ■	0.34 ■	0.73 ■

Guidelines for agreement (Landis & Koch, 1977): ■ < 0.2: poor, ■ 0.2–0.4: fair, ■ 0.4–0.6: moderate, ■ 0.6–0.8: substantial, ■ > 0.8: almost perfect

a and ρ estimates. The correlations we see here agree with the findings of (Barazany et al., 2009) and (Alexander et al., 2010). While MD is not correlated either of the microstructure indices, the directional diffusivities AD and RD both show moderate correlations with a and ρ. Of course it is not surprising to find RD negatively correlated with a and positively correlated with ρ respectively, as it is know both axonal packing density, and axon diameter all influence RD measurements (Beaulieu, 2002). The observed correlation between AD and a (positive) and ρ (negative) is less intuitively explainable, however consistent with previous findings (Barazany et al., 2009; Alexander et al., 2010). Alexander et al. speculate that the increase of axon size and decrease of packing density are associated with lower fibre coherency, and thus are causing an increasing amount of diffusion impedance along the dominant diffusion direction. The correlation between AD and the a and ρ indices might also be the result of varying CSF contamination, since the regions high axon diameter are mostly found in the thinner midbody region are more affected by partial volume effects than those in genu and splenium. Since we find both AD and RD correlated with the a and ρ indices, their correlation with FA follows by definition.
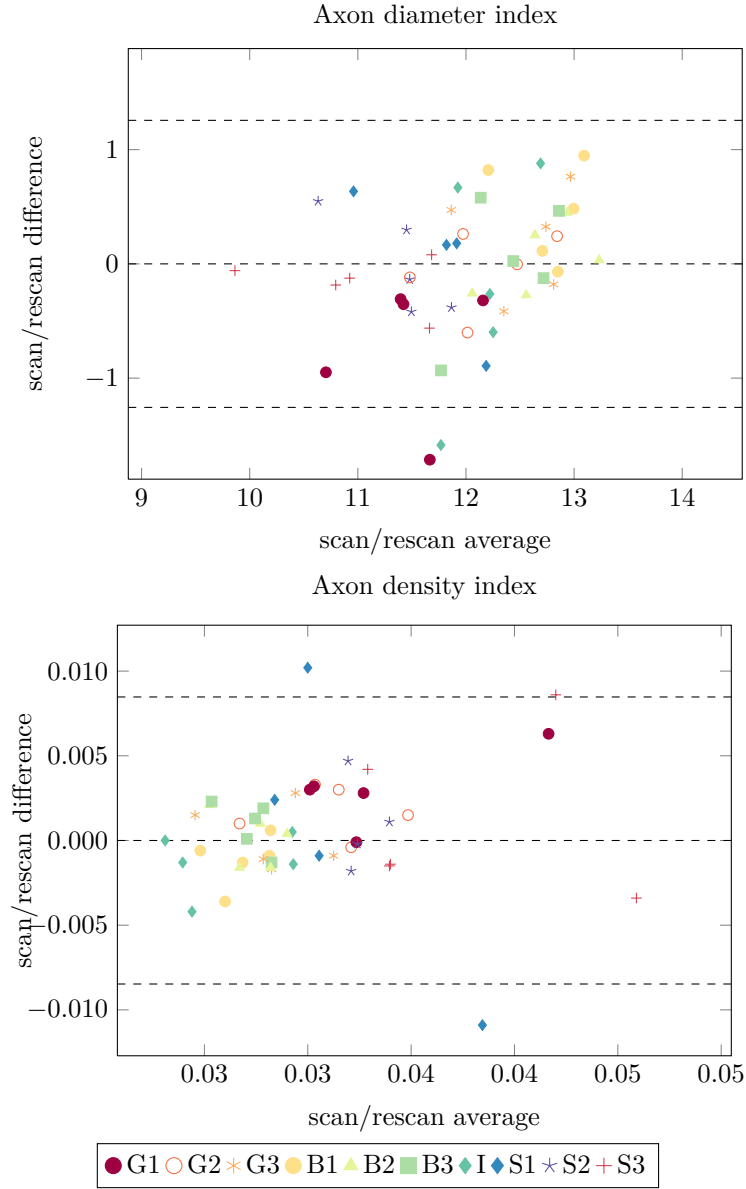
Axon diameter index

Axon density index

Figure 1.6: Bland-Altman scan/rescan reproducibility analysis of a and ρ in all CC ROIs.
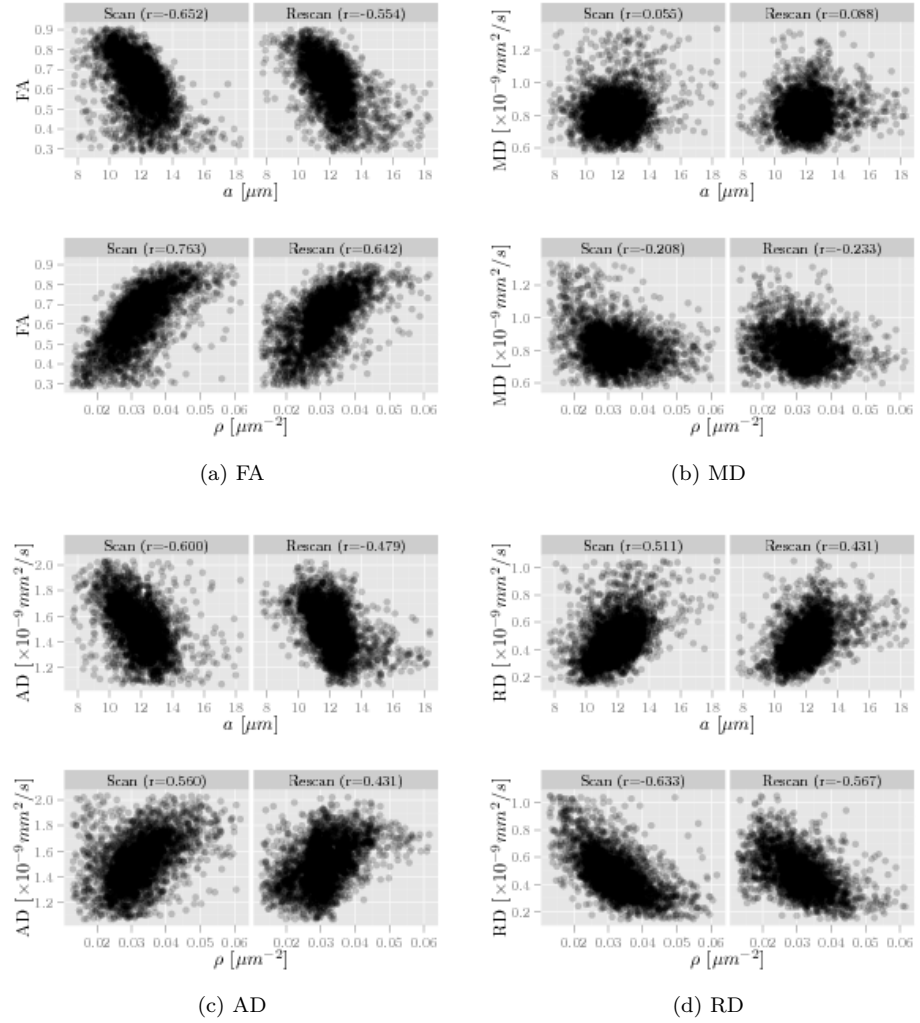
(a) FA

(b) MD

(c) AD

(d) RD

Figure 1.7: Scatterplots of DTI metrics and a and ρ. The r value denotes the correspondenceding correlation coefficient.

Axon diameter and axon density indices in the SC

Figure 1.8 shows the a and ρ maps acquired in one healthy volunteer. We clearly see the bilateral symmetry of the parameter maps as expected from the basic anatomy of the spinal cord. The estimates of a and ρ indices are within a similar range of values measured in the CC. Furthermore, both a and ρ allow good discrimination between motor and sensory WM tracts. The largest a ($10.7 \pm 2\mu m$) and lowest ρ ($0.035 \pm 0.017 \mu m^{-2}$) are found in the lateral tract. The dorsal sensory tract shows the lowest a ($9.1 \pm 1.3 \mu m$) and highest ρ ($0.046 \pm 0.017 \mu m^{-2}$). The contrast between LT and DC is consistent over several slices in our dataset and agrees with our earlier findings in fixed monkey cervical cord. Figure 1.8 also illustrates well the challenges in SC imaging. The posterior halo of low a is the result of motion artifacts during the acquisition which can be cause e.g. by swallowing or breathing. Cardiac motion also makes cardiac gating a neccesity, which in turn reduces the data we can acquire within the 25 minute windows and consequently reduced the SNR in our data. However, the results here show first evidence that our $a\mathcal{SF}$ protocol can be used successfully in the SC application, despite the more challenging imaging environment.
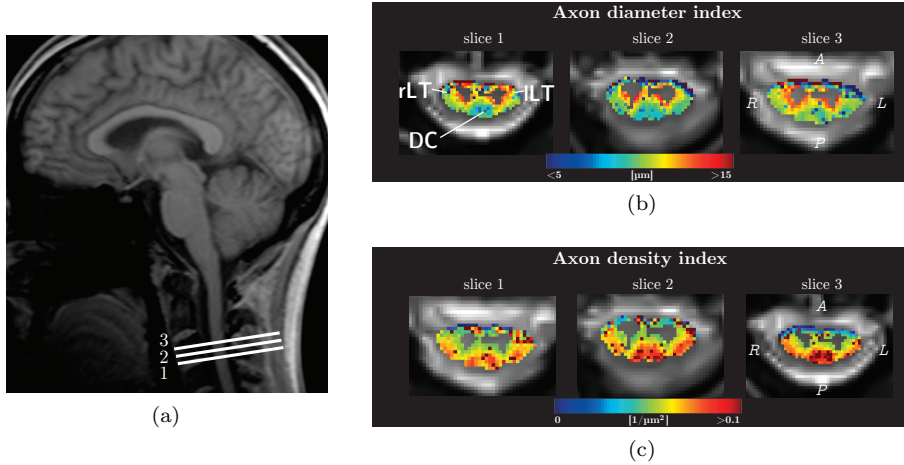

Figure 1.8: (a) SC slice alignment and (b&c) maps of a and ρ in one healthy volunteer. Annotations on the first result slice denote the location of the dorsal column (DC) and left and right lateral tracts (LT).

1.4 Discussion

This work presents a novel imaging and analysis pipeline for measuring axon diameter and density indices in the CC in-vivo, which expands on our $a\mathcal{SF}$ protocol optimisation we introduced in the previous chapter. We combined small FOV imaging and careful optimisation of the MR protocols and post-processing techniques to gain both high spatial resolution while maximising SNR. We show here axon diameter and axon density maps of better quality than previous studies have shown before. For the first time present results of a larger subject cohort of 5 subjects, allowing to infer scan and rescan reproducibilty with more

confidence. Our results show that a and ρ show very good reproducibility consistently over all investigated subjects. Furthermore, a first test of our protocol in healthy cervical produced compelling results that are in good agreement with our findings excised monkey cervical cord.

Limitations & further work

Interpretation of a and ρ   The model we use here is a very simplistic approximation of the complex micro-anatomy of real biological tissue. The actual estimates of axon diameter and densities differ considerably from what is expected from histology or ex-vivo scans (Alexander et al., 2010). Most of this disparity can be explained by the limited gradient strength available on clinical system. With limited gradient strength, small axons cause very little signal attenuation and become indistinguishable from each other (Lätt et al., 2007; Yeh et al., 2010). Our simulation experiments in Chapter **??** show a limit of sensitivity of of 2–$4\mu m$ even in the very idealised situation of perfectly aligned single-radius cylinders. Consequently, the a and ρ indices must not be seen as accurate reflections of the complete axon diameter distribution as they are likely driven only by a small number of large axons in the WM.

Other more complex models have been also been suggested, adding more tissue compartments, a distribution of axon diameters and/or permeable membranes. However, with the given limits both in scan time and gradient hardware, their practical value for in-vivo clinical applications is questionable. Recent studies e.g. by Panagiotaki et al. (2012); Ferizi et al. (2012) have studied those more complex models in the CC WM tissue with much more extensive datasets than we used here. Their findings suggest that a simple two compartment model similar to ours explains diffusion in coherent WM tissue reasonably well. For our purpose of clinical adaptation, this model provides the best trade-off between explaining the diffusion in WM while keeping data requirements reasonably low. Furthermore, the shorter protocol we propose is an important step to enable more widespread adaptation of our imaging pipeline, which in turn will lead to a better understanding of its parameters interpretation.

Furthermore, alternative acquisition methods such as oscillating gradients (Does et al., 2003; Colvin et al., 2008) or multiple wave-vector acquisitions (Komlosh et al., 2008; Koch & Finsterbusch, 2008; Avram et al., 2012) promise more sensitivity to smaller axon diameters. Recently the protocol optimisation framework has been extended to support such non-rectangular gradient waveformsDrobnjak et al. (2010); Siow et al. (2012). The method we present here is seasily combined with any other pulse sequences to provide better discrimination of small axon diameters.

T2 estimation: We chose here to estimate T2 directly from the b=0 weighted images. Using this approach, we are limited to estimate rather high TEs due to the nature of the single shot EPI technique used here. Furthermore, due to the sparsity of the TEs samples, we can only account for mono-exponential T2-decay. A more comprehensive T2 decay curve could potentially be estimated using the Carr-Purcell-Meiboom-Gill (CPMG) sequence (Pell et al., 2006). However, this approach would add significant scan time to our protocol. Furthermore, such acquisition does not suffer from the same image distortions as the EPI DWI images and therefore requires further registration, which might

confound the results. Nevertheless, a better T2 decay curve estimate might also be used to correct for T2 differences between intra- and extra-axonal compartments. Fitting a single T2 to all compartments could lead to errors in the f_{intra} estimates and might have an affect on our ρ parameter maps. While we focussed on a single-compartment T2 estimation that to simply fitting, our tissue model can easily incorporate different T2s for individual compartments.

Validation: We have validate our result here by comparision with previous reports of tissue parameter estimates by diffusion MRI and independent histopathology. While several systematic reports of the tissue microstructure are available in the CC, validation of our results is more complicated in the SC as it is much less documented. Future work needs is required that provides a direct comparison between our MRI parameters and independent histology for a better interpretation of our estimated parameters in healthy tissue but more importantly also in the presence of pathological tissue alteration. Following up on our work on $a\mathcal{SF}$, we are now in the process of setting a validation study of our protocol using post-mortem human spinal cord of healthy and MS tissue in collaboration with Dr DeLuca from the Nuffield Department of Neurosciences, University of Oxford.

Clinical application: The protocols we present here are designed with clinical adaptation in mind. Due ot the short acquisition time, our 25 minute protocol can be easily incorporated into existing studies. A disadvantage of our method is that it does not offer whole brain coverage. However, the alternative $\mathcal{OI}$ method is also intrinsically limiting by the tissue model to application in highly coherent WM structures. In fact, if only such structures are to be studies anyway, our method provides much better spatial resolution, SNR in shorter acquisition time. Furthermore, many neurological diseases such as Alzheimers disease, Schizophrenia or MS have severe impact on the CC and diagnosis. In those diseases, diagnosnis and therapy monitoring might benefit from better tissue characterisation. Furthermore, the first results in the SC we showed also promise future application in the cord, e.g. to gain better biomarkers for diagnosis and therapeutic outcome in SCI. Wider application in other parts in the CNS might come from the adaption of a more complex tissue model which incorporates fibre dispersion and fibre crossing Zhang et al. (2011).

1.5 Conclusion

We have demonstrated that our microstructure estimates agree with reported post-mortem evaluation of the CC fibre density distribution. Further, we showed good inter- and intra-subject reproducibility. The scan time of the protocol is short enough to be easily incorporated into clinical studies. In future work, we are planning to use this approach in subjects with known altered microstructure of the CC.

Bibliography

Aboitiz, F., Scheibel, A. B., Fisher, R. S., & Zaidel, E. (1992). Individual differences in brain asymmetries and fiber composition in the human corpus callosum. *Brain Research*, *598*(1-2), 154â 161.

Alexander, D. C., Hubbard, P. L., Hall, M. G., Moore, E. A., Ptito, M., Parker, G. J. M., & Dyrby, T. B. (2010). Orientationally invariant indices of axon diameter and density from diffusion MRI. *NeuroImage*.

Avram, A. V., √ñzarslan, E., Sarlls, J. E., & Basser, P. J. (2012). In vivo detection of microscopic anisotropy using quadruple pulsed-field gradient (qPFG) diffusion MRI on a clinical scanner. *NeuroImage*, (0).
URL `http://www.sciencedirect.com/science/article/pii/S1053811912008567`

Barazany, D., Basser, P. J., & Assaf, Y. (2009). In vivo measurement of axon diameter distribution in the corpus callosum of rat brain. *Brain*.

Beaulieu, C. (2002). The basis of anisotropic water diffusion in the nervous system - a technical review. *NMR in Biomedicine*, *15*(7-8), 435â 455.

Colvin, D. C., Yankeelov, T. E., Does, M. D., Yue, Z., Quarles, C., & Gore, J. C. (2008). New insights into tumor microstructure using temporal diffusion spectroscopy. *Cancer Research*, *68*(14), 5941–5947.
URL `http://cancerres.aacrjournals.org/content/68/14/5941.short`

Cook, P., Bai, Y., Nedjati-Gilani, S., Seunarine, K., Hall, M. G., Parker, G. J. M., & Alexander, D. C. (2006). Camino: open-source diffusion-MRI reconstruction and processing. In *Proceedings 14th Scientific Meeting, International Society for Magnetic Resonance in Medicine*, (p. 2759).

Does, M. D., Parsons, E. C., & Gore, J. C. (2003). Oscillating gradient measurements of water diffusion in normal and globally ischemic rat brain. *Magnetic Resonance in Medicine*, *49*(2), 206,Äì215.
URL `http://onlinelibrary.wiley.com/doi/10.1002/mrm.10385/abstract`

Drobnjak, I., Siow, B., & Alexander, D. C. (2010). Optimizing gradient waveforms for microstructure sensitivity in diffusion-weighted MR. *Journal of Magnetic Resonance*, *206*(1), 41â 51.

Ferizi, U., Panagiotaki, E., Schneider, T., Wheeler-Kingshott, C., & Alexander, D. C. (2012). White matter models of in vivo diffusion mri human brain data:

A statistical ranking. In *16th Conference on Medical Image Understanding and Analysis.*

Huber, P. J. (1996). *Robust Statistical Procedures.* SIAM.

Koch, M. A., & Finsterbusch, J. (2008). Compartment size estimation with double wave vector diffusion-weighted imaging. *Magnetic Resonance in Medicine.*

Komlosh, M., Lizak, M., Horkay, F., Freidlin, R., & Basser, P. (2008). Observation of microscopic diffusion anisotropy in the spinal cord using double-pulsed gradient spin echo MRI. *Magnetic Resonance in Medicine*, *59*(4), 803‚Äì809.
URL   http://onlinelibrary.wiley.com/doi/10.1002/mrm.21528/abstract

Landis, J. R., & Koch, G. G. (1977). The measurement of observer agreement for categorical data. *Biometrics*, *33*(1), 159.
URL   http://www.jstor.org/discover/10.2307/2529310?uid=3738032&uid=2&uid=4&sid=21101301805217

Lätt, J., Nilsson, M., Malmborg, C., Rosquist, H., Wirestam, R., St\aa hlberg, F., Topgaard, D., & Brockstedt, S. (2007). Accuracy of q-space related parameters in MRI: simulations and phantom measurements. *IEEE Transactions on Medical Imaging*, *26*(11), 1437â 1447.

Modat, M., Ridgway, G. R., Taylor, Z. A., Lehmann, M., Barnes, J., Hawkes, D. J., Fox, N. C., & Ourselin, S. (2010). Fast free-form deformation using graphics processing units. *Computer Methods and Programs in Biomedicine*, *98*(3), 278–284.
URL   http://www.sciencedirect.com/science/article/pii/S0169260709002533

Ourselin, S., Roche, A., Subsol, G., Pennec, X., & Ayache, N. (2001). Reconstructing a 3D structure from serial histological sections. *Image and Vision Computing*, *19*(1,Äì2), 25–31.
URL   http://www.sciencedirect.com/science/article/pii/S0262885600000524

Panagiotaki, E., Schneider, T., Siow, B., Hall, M. G., Lythgoe, M. F., & Alexander, D. C. (2012). Compartment models of the diffusion MR signal in brain white matter: A taxonomy and comparison. *NeuroImage*, *59*(3), 2241â 2254.
URL   http://www.sciencedirect.com/science/article/pii/S1053811911011566

Pell, G. S., Briellmann, R. S., Waites, A. B., Abbott, D. F., Lewis, D. P., & Jackson, G. D. (2006). Optimized clinical t2 relaxometry with a standard CPMG sequence. *Journal of Magnetic Resonance Imaging*, *23*(2), 248,Äì252.
URL   http://onlinelibrary.wiley.com/doi/10.1002/jmri.20490/abstract

R Core Team (2012). *R: A Language and Environment for Statistical Computing.*
R Foundation for Statistical Computing, Vienna, Austria. ISBN 3-900051-07-0.
URL `http://www.R-project.org/`

Shrout, P. E., & Fleiss, J. L. (1979). Intraclass correlations: Uses in assessing
rater reliability. *Psychological Bulletin*, *86*(2), 420–428.

Siow, B., Ianus, A., Drobnjak, I., Lythgoe, M. F., & Alexander, D. C. (2012).
Optimised oscillating gradient diffusion mri for the estimation of axon radius
in an ex vivo rat brain. In *Proceedings 20th Scientific Meeting, International
Society for Magnetic Resonance in Medicine.*

Tristán-Vega, A., Garcia-Pérez, V., Aja-Fernández, S., & Westin, C.-F. (2012).
Efficient and robust nonlocal means denoising of MR data based on salient
features matching. *Computer Methods and Programs in Biomedicine*, *105*(2),
131–144.
URL `http://www.sciencedirect.com/science/article/pii/`
`S0169260711002021`

Wang, J., Zamar, R., Marazzi, A., Yohai, V., Salibian-Barrera, M., Maronna,
R., Zivot, E., Rocke, D., Martin, D., Maechler, M., & Konis., K. (2012).
robust: Insightful Robust Library. R package version 0.3-19.
URL `http://CRAN.R-project.org/package=robust`

Wilm, B., Svensson, J., Henning, A., Pruessmann, K., Boesiger, P., & Kollias,
S. (2007). Reduced field-of-view MRI using outer volume suppression for
spinal cord diffusion imaging. *Magnetic Resonance in Medicine*, *57*(3),
625â 630.
URL `http://onlinelibrary.wiley.com/doi/10.1002/mrm.21167/`
`abstract`

Wolak, M. E., Fairbairn, D. J., & Paulsen, Y. R. (2011). Guidelines for estim-
ating repeatability. *Methods in Ecology and Evolution.*

Yeh, C.-H., Tournier, J.-D., Cho, K.-H., Lin, C.-P., Calamante, F., & Connelly,
A. (2010). The effect of finite diffusion gradient pulse duration on fibre
orientation estimation in diffusion MRI. *NeuroImage*, *51*(2), 743–751.
URL `http://www.sciencedirect.com/science/article/pii/`
`S1053811910002090`

Zhang, H., Hubbard, P. L., Parker, G. J., & Alexander, D. C. (2011). Axon
diameter mapping in the presence of orientation dispersion with diffusion
MRI. *NeuroImage*, *56*(3), 1301â 1315.
URL `http://www.sciencedirect.com/science/article/pii/`
`S1053811911001376`